# Finite Element Solutions of Euler Equations for Lifting Airfoils

H. U. Akay,* A. Ecer,* and P. G. Willhite†
*Purdue University at Indianapolis, Indianapolis, Indiana*

**A Clebsch formulation of Euler equations that includes the isentropic potential, as well as the nonisentropic potential assumptions as special cases, is applied to transonic flows around airfoils using finite elements. The implementation of the Kutta condition at the sharp trailing edges for potential and Euler equations is presented. The differences for all three levels of approximations are discussed: isentropic potential, nonisentropic potential, and full Euler. It is shown that the present formulation provides a unified approach for comparing the effect of each of these approximations on the numerical results.**

## Introduction

THE analysis of inviscid transonic flows has attracted considerable attention during the last 15 years. Initially, most of the efforts were directed toward the solution of potential flows. More recently, however, the Euler solutions of transonic flows have become almost as popular. In comparing the solutions, two basic arguments are often made. The first is related to the efficiency in obtaining the numerical results. Potential solutions are obtained through the use of relaxation schemes and involve the determination of a single variable—the velocity potential function. Euler equations are generally cast in terms of the primitive variables—the velocity components and the mass density. They usually require a timewise integration of unsteady Euler equations. Both in terms of the speed of convergence and number of variables, they are generally less efficient for solving a particular transonic flow problem. On the other hand, potential flow equations are restricted to isentropic flows and ignore the effects of rotationality. As is also illustrated in this paper, the entropies generated at the shocks and their effects downstream of the shocks have been found to be important, even for moderately strong shock waves.[1] One can question the accuracy of isentropic potential solutions since they can produce deviations from the Euler solutions, even for simple two-dimensional flows around airfoils. Recently, attempts have been made to improve the accuracy of the potential solutions by including the entropy increases across the shocks into the equations as density corrections,[2-4] while still keeping the irrotational flow assumption. Nonisentropic potential flow solutions can then be obtained with the shock strengths calculated more accurately due to the inclusion of entropy generations and rotationalities.

The comparison of the potential and Euler solutions, in terms of accuracy, however, is not a straightforward task. The discretization errors due to the artificial viscosity are difficult to determine, since the basic equations are cast in entirely different forms: velocity potential versus primitive variables. The objective of the present paper is to study the relative accuracy of the potential and Euler solutions in solving transonic flow problems using a formulation that includes the potential solution as a subset. The method considered for the analysis involves a Clebsch representation of the velocity field in the following form:

$$\boldsymbol{u} = \nabla\phi + \alpha\nabla\beta \tag{1}$$

where $\phi$ and $\beta$ are some scalar functions and $\alpha$ the material coordinate. Since for steady inviscid flows, the entropy remains constant on constant $\alpha$ lines, i.e., $S = S(\alpha)$, when the entropy gradients are assumed to be zero, the formulation reduces to the solution of a single equation in terms of the scalar variable $\phi$ known as the velocity potential function. The applications of this method to nonlifting transonic flows have been presented earlier[5-7] using the finite element method. An extension of the method to the case of lifting airfoils is considered in the present paper.

Two transonic test cases are presented for the flow around a NACA 0012 airfoil with different inflow Mach numbers and angles of attack. Using the same computational grid, three types of solutions are obtained: isentropic potential, nonisentropic potential, and a full Euler. As will be discussed, these three solutions appear successively in the present solution scheme. In each case, the Kutta condition around the sharp trailing edge was modeled consistently. The artificial viscosity is introduced by upwinding the density in all three cases. Except for the upwinding of the density at the supersonic regions, no other diffusion terms are added to the Euler equations. The present method provides a measure of relative errors in modeling the different aspects of transonic flows.

## Method of Solution

When a Clebsch transformation of the velocity vector as shown in Eq. (1) is used, Euler equations for steady isoenergetic flows take the following form[5-7]:

$$\nabla\cdot(\rho\boldsymbol{u}) = 0 \tag{2}$$

$$\rho\boldsymbol{u}\cdot\nabla\beta = -(p/R)S_{,\alpha} \tag{3}$$

$$\rho\boldsymbol{u}\cdot\nabla\alpha = 0 \tag{4}$$

using the variables $\phi$, $\alpha$, $\beta$, and the equation of state

$$p = \kappa\rho^{\gamma}e^{(\gamma-1)S/R} \tag{5}$$

where

$$S = S(\alpha) \tag{6}$$

The above equations can be shown to be equivalent to a more familiar form expressed in terms of the primitive variables $\boldsymbol{u}$, $\rho$, and $S$. The vorticity vector $\zeta$ with the Clebsch variables can be written as

$$\zeta = \nabla\times\boldsymbol{u} = \nabla\alpha\times\nabla\beta \tag{7}$$

The above set of Euler equations require the specification of the normal mass flux on all boundaries and the specifica-

Presented as Paper 85-0294 at the AIAA 23rd Aerospace Sciences Meeting, Reno, NV, Jan. 14-17, 1985; received Feb. 11, 1985; revision received July 18, 1985. 

*Professor of Mechanical Engineering. Member AIAA.
†Research Assistant.

tion of $\alpha$ and $\beta$ at the freestream inflow boundaries. For uniform inflow conditions, when $\beta$ is set to a constant, the irrotationality condition at the inlet $\zeta=0$ is satisfied from Eq. (7). The entropy distributions $S=S(\alpha)$ after a shock wave can be determined from Rankine-Hugoniot shock jump conditions.[5-7]

For obtaining numerical solutions, Eqs. (3) and (4) are further cast into a second-order form as described in Refs. 5-7. The resulting equations are solved by using the finite element method with a second-order accuracy except for the upwinding of the density in the supersonic regions.[5-7] For analyzing isentropic flows, only the solution of Eq. (2) is required. By using the equations of state, one can further express the mass density as follows:

$$\rho=c\theta(H-\tfrac{1}{2}\boldsymbol{u}\cdot\boldsymbol{u})^{\theta-1}e^{-S/R} \tag{8}$$

and the static pressure as

$$p=c(H-\tfrac{1}{2}\boldsymbol{u}\cdot\boldsymbol{u})^{\theta}e^{-S/R} \tag{9}$$

where $H$ is the stagnation enthalpy (a constant) and

$$\theta=\gamma/(\gamma-1), \quad c=\kappa(\kappa\theta)^{-\theta} \tag{10}$$

In the case of isentropic flows, the mass density and the static pressure do not vary with the entropy, thus $S$ may be set to zero in Eqs. (8) and (9).

The main steps of the solution scheme can be summarized as follows:

Step 1: isentropic potential flow approximation. Assuming an isentropic flow, Eq. (2) is solved by using a finite element relaxation scheme, while upwinding the mass density inside the supersonic pockets.[8] The Kutta condition is imposed at the sharp trailing edge of the airfoil by using a model described in the following section. The relaxation scheme is continued until the solution converges, while the static pressures and consequently the velocities on both sides of the trailing edge are equalized. This yields an irrotational and isentropic (potential) solution in which $\boldsymbol{u}=\nabla\phi$ and $S=$const (i.e., $S=0$) everywhere during the density and pressure computations of Eqs. (8) and (9), respectively.

Step 2: nonisentropic potential flow approximation. Starting with the previously obtained solution of step 1, the mass densities downstream of the shock are modified using the predicted entropy jumps across the shock. Since for steady, inviscid flows, the entropy along each material line is constant, the entire $S=S(\alpha)$ distribution is determined by solving Eq. (4) in conjunction with the Rankine-Hugoniot relationship. The corrections may be introduced iteratively by successively solving Eqs. (2) and (4). However, by solving Eq. (4) only once, following the potential solution, one can obtain a good estimate of the material lines as a first approximation to the problem. This corresponds to assuming that the streamlines do not vary significantly after the isentropic potential solution. It is also possible to obtain seldom updates on material lines by solving Eq. (4) after several iterations of Eq. (2). In this approximation, the velocity field is still irrotational, i.e., $\boldsymbol{u}=\nabla\phi$, while the entropy variations from one streamline to another are considered during the density computations in Eq. (8) following a shock wave. The Kutta condition is imposed to equalize the static pressures on both sides of the trailing edge. The relaxation scheme is continued until the solutions converge and the static pressures on both sides of the wake are equalized. Equation (3) is not employed in this case.

Step 3: full Euler approximation. Using the complete Clebsch transformation in Eq. (1), Eqs. (2-4) are solved successively, while predicting the entropy distribution along the shock lines from the Rankine-Hugoniot relationship. The Kutta condition is applied to equalize the static pressures on both sides of the airfoil trailing edge. The relaxation scheme is continued until solutions for all three variables $\phi$, $\alpha$, and $\beta$ converge.

The differences between the numerical results obtained from steps 1 and 2 mainly depend on the strength of the shock. On the other hand, the differences between steps 2 and 3 are due to the changes in streamlines or material lines caused by the rotationality of the flow.

Two previously reported solutions of transonic Euler equations involved flows over a bump in a channel.[5,6] In both of these cases, because the rotationalities were small, i.e.,

$$|\nabla\phi| \gg |\alpha\nabla\beta| \tag{11}$$

the velocity vector can be approximated as

$$\boldsymbol{u}\simeq\nabla\phi \tag{12}$$

For these problems, the main differences between the potential Euler solutions are primarily due to the corrections in the density from the entropy rise across the shock. Therefore, the flowfield can be approximated quite accurately by an irrotational field. The rate of convergence of the relaxation scheme for the Euler equations is then basically the same as for the potential relaxation schemes.

When cases with higher rotationality are considered, however, such an approximation may not be satisfactory. In the case of transonic flow over a semicircular cylinder,[7] for example, the approximations in Eqs. (11) and (12) are no longer valid. The rotational components of the velocity field become quite important and, in fact, they change the entire flowfield behind the cylinder.[7] The rate of convergence of the relaxation scheme for such flows is slower due to the additional nonlinearities in the velocity field in Eq. (1).

In the present paper, attention is given for analyzing flows around lifting airfoils. Since the accuracy of determining the lift for such an airfoil is of major concern, the importance of different parameters in the formulation is considered. Also, the imposition of the Kutta condition for different approximations is studied in detail.

## Application of the Kutta Condition

In the case of potential flows, the boundary conditions are specified only in terms of the normal mass flux

$$f=\rho\boldsymbol{u}\cdot\boldsymbol{n} \tag{13}$$

on the boundaries, where $\boldsymbol{n}$ denotes an outward unit normal vector on the boundary. For the case of an airfoil in a flowfield, however, a unique solution requires the specification of the tangential velocity distribution around the airfoil surface $B$ to yield the correct circulation

$$\Gamma=\oint_B \boldsymbol{u}\cdot\mathrm{d}\boldsymbol{s} \tag{14}$$

For an airfoil with a sharp trailing edge, this circulation is imposed by assuming that the flow speed at the trailing edge is finite and that the streamlines on the upper and lower surfaces of the airfoil leave the trailing edge smoothly with a continuous pressure distribution. When the flow is isentropic, this is also the equivalent to imposing that the velocities be equalized on both sides of the sharp trailing edge.

A cut in the computational grid extending from the trailing edge to the downstream boundary is employed as shown in Fig. 1 in applying the Kutta condition. Here, the cut models a streamline originating from the trailing edge of the airfoil. In this figure, $E$ denotes the trailing-edge point, + and − denote the upper and lower surfaces of the dividing streamline, respectively, and $s$ and $n$ are the tangential nor-

mal directions of this streamline. Using this model, the Kutta condition for each approximation is imposed iteratively as described in the following.

**Isentropic Potential Flow Approximation**

At the trailing edge of the airfoil, there are two independent nodes $E^+$ and $E^-$, from which a jump in the velocity potential is calculated at each step as

$$\Delta\phi = \phi_E^+ - \phi_E^- \tag{15}$$

Since $u = \nabla\phi$, this jump can be shown to be related to the circulation over the airfoil from Eq. (14) as

$$\Delta\phi = -\Gamma \tag{16}$$

the same jump is imposed on all pairs of nodes along the cut by setting

$$\phi^+ = \phi^- + \Delta\phi \quad \text{on } F\,G \tag{17}$$

Thus, the total circulation is constant on all contours enclosing the airfoil. This produces the following conditions across the cut:

$$u_n^+ = u_n^- = 0 \quad \text{on } E\,F \tag{18}$$

$$\rho u_n^+ = \rho u_n^- \quad \text{on } F\,G \tag{19}$$

and

$$u_s^+ = u_s^- \quad \text{on } E\,G \tag{20}$$

where $u_s$ and $u_n$ denote, respectively, the tangential and normal components of the velocity vector along the cut. Thus, in view of Eqs. (18) and (20), the velocities and static pressure at the trailing-edge point $E$ are equalized, which gives the correct Kutta condition. Also, with increasing grid refinements, the stagnation point is constrained to move closer to the trailing edge. In the case of isentropic potential flows, the cut does not have to follow a streamline since no flow variable is discontinuous across the streamlines.

**Nonisentropic Potential Flow Approximation**

When the flow is nonisentropic, the streamlines following the upper and lower surface of the airfoil do not convect the same entropy due to differing shock strengths. Consequently, a tangential discontinuity is formed along the cut (dividing streamline). The definition of a streamline requires that

$$u_n^+ = u_n^- = 0 \tag{21}$$

while the balance of momentum fluxes normal to the streamline yields the condition

$$p^+ = p^- \tag{22}$$

on $E\,G$. Equation (4) requires the entropy distribution to be continuous only along a streamline. Thus, the tangential velocity $u_s$, the mass density $\rho$, and the entropy $S$ may be discontinuous across a streamline. Although the exact position of the dividing streamline is usually unknown, for small angles of attack in which $|u_y| \ll |u_x|$, we may still assume that it extends horizontally. Using Eq. (9), the tangential discontinuities in velocity are computed from the equal pressure conditions $p^+ = p^- = p$ along the dividing streamline as follows:

$$\Delta u_s = u_s^+ - u_s^- = \{2[H - (p/c)^{1/\theta}\exp^{S^+/R\theta}]\}^{1/2} - \{2[H - (p/c)^{1/\theta}\exp^{S^-/R\theta}]\}^{1/2} \tag{23}$$

Since the flow is assumed to be irrotational (i.e., $u = \nabla\phi$), the jump in the velocity potential across the dividing streamline shown in Fig. 1 is calculated from

$$\Delta\phi(s) = \int_0^s u_s ds + \Delta\phi(0) \tag{24}$$

where

$$\Delta\phi(0) = (\phi_E^+ - \phi_E^-) \tag{25}$$

A simple numerical integration scheme is employed to perform the integral in Eq. (24). Using this jump in the $\phi$ values, the velocity potentials on the upper surface of the dividing streamline are specified as

$$\phi^+(s) = \phi^-(s) + \Delta\phi(s) \tag{26}$$

The circulation around the airfoil is again given by

$$\Gamma = -(\phi_E^+ - \phi_E^-) \tag{27}$$

However, it varies on all other closed contours enclosing the airfoil due to the additional circulation introduced by the velocity jump across the dividing streamline.

**Full Euler Approximation**

In this approximation the conditions set by Eqs. (21-23) still hold. But, since the Clebsch representation

$$u = \nabla\phi + \alpha\nabla\beta \tag{28}$$

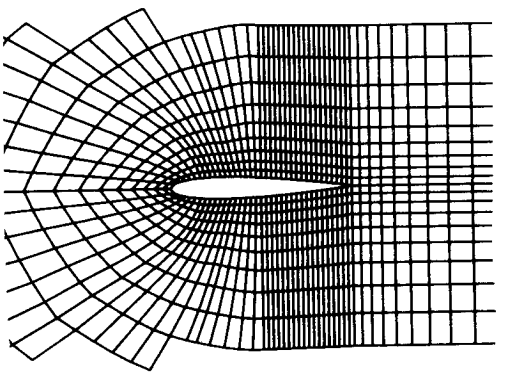

**Fig. 2 Finite element grid (only the details around the airfoil are shown).**

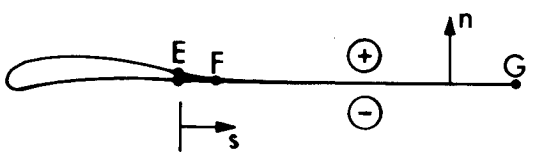


**Fig. 1 Kutta condition model and the dividing streamline.**

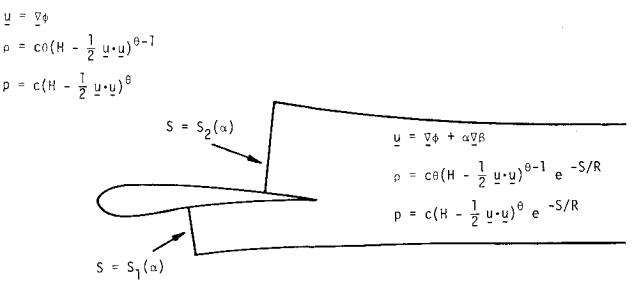


**Fig. 3 Irrotational and rotational flow regions around an airfoil.**

is used, the jump in the velocity potential is determined from

$$\Delta\phi(s) = \int_0^s \Delta u_s ds - \int_0^s \alpha \Delta\beta_{,s} ds + \Delta\phi(0) \tag{29}$$

where

$$\Delta\phi(0) = (\phi_E^+ - \phi_E^-) \tag{30}$$

and

$$\Delta\beta_{,s} = \beta_{,s}^+ - \beta_{,s}^- \tag{31}$$

Also by employing Eq. (3), one can write

$$\beta_{,s}^+ = -(pS_{,\alpha}^+)/(\rho^+ u_s^+ R) \tag{32}$$

$$\beta_{,s}^- = -(pS_{,\alpha}^-)/(\rho^- u_s^- R) \tag{33}$$

The Clebsch variables along the upper surface of the dividing streamline are specified as

$$\phi^+(s) = \phi^-(s) + \Delta\phi(s) \tag{34}$$

$$\beta^+(s) = \beta^-(s) + \int_0^s \Delta\beta_{,s} ds \tag{35}$$

$$\alpha^+(s) = \alpha^-(s) = \alpha(s) \tag{36}$$

Thus, while $\phi$ and $\beta$ are discontinuous across the dividing streamline, $\alpha$ remains continuous. The circulation around the airfoil is obtained from

$$\Gamma = -(\phi_E^+ - \phi_E^-) - \alpha(\beta_E^+ - \beta_E^-) \tag{37}$$

while it varies on all other closed contours enclosing the airfoil.

In obtaining the following numerical results, the discontinuity past the trailing edge was assumed to remain along a horizontal line. However, in nonisentropic flows, due to different stagnation pressures (i.e., different shock strengths) on the upper and lower surface streamlines of the airfoil, the flow leaves the trailing edge tangentially to one surface. Therefore, the dividing streamline is not horizontal. This streamline can be determined at each iteration from the most recently calculated $\alpha$ values and the grid points can consequently be moved to match the correct streamline. For the present test cases, since the variations in flow directions behind the trailing edge were relatively small, no such grid modifications were made.

## Discussion of Results

To demonstrate the basic differences between the solutions of potential and Euler equations, two test cases were chosen. These cases involve the analysis of transonic flows around a NACA 0012 airfoil with different freestream Mach numbers and angles of attack, where for case 1 $M_\infty = 0.80$ and $\beta_\infty = 1.25$ deg and for case 2 $M_\infty = 0.85$ and $\beta_\infty = 1.0$ deg. Here, $M_\infty$ and $\beta_\infty$ denote, respectively, the Mach number and angle of attack at the freestream. These two problems were also chosen as basic test cases for comparing potential and Euler solution schemes at a GAMM Workshop on tran-

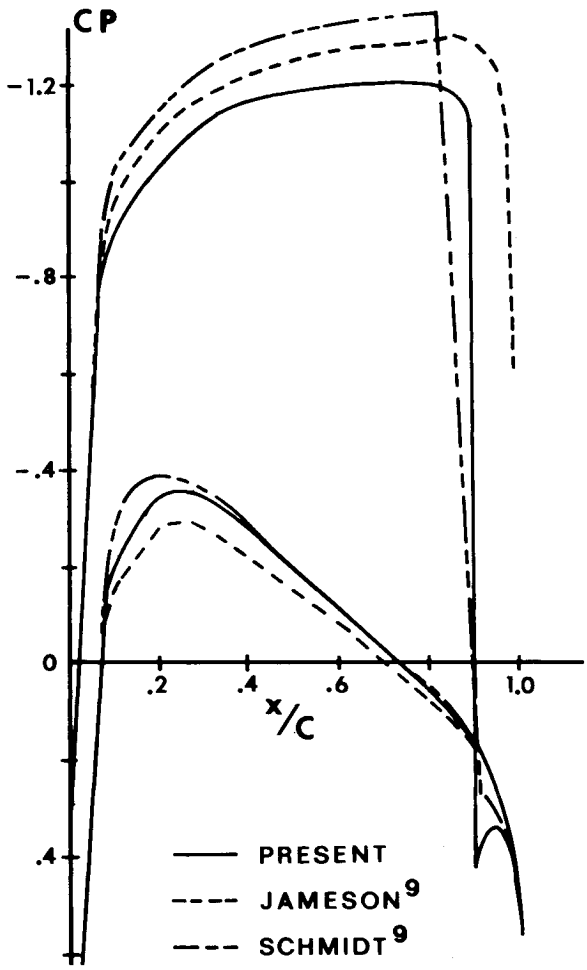


Fig. 4 Comparison of pressure coefficients for isentropic potential solutions ($M_\infty = 0.80$, $\beta_\infty = 1.25$ deg).

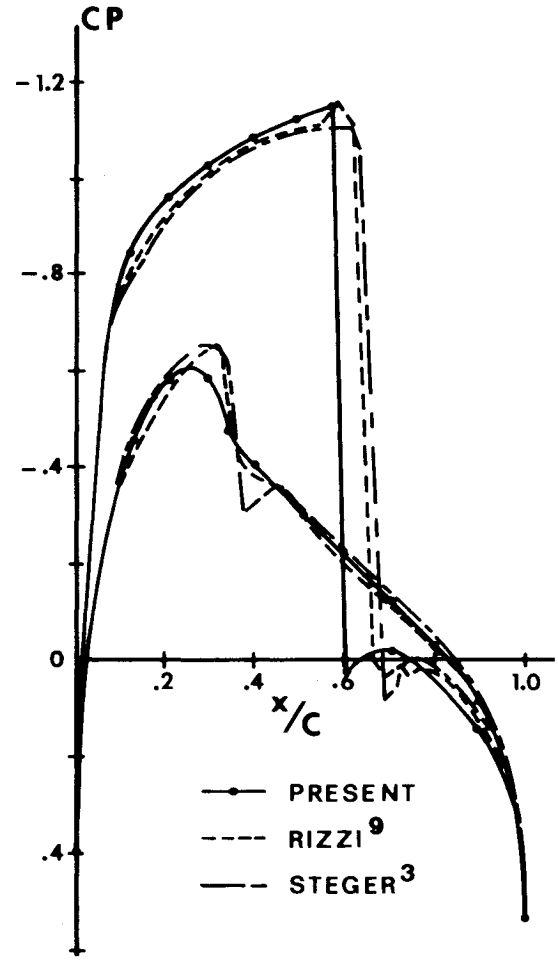


Fig. 5 Comparison of pressure coefficients for Euler solutions ($M_\infty = 0.80$, $\beta_\infty = 1.25$ deg).

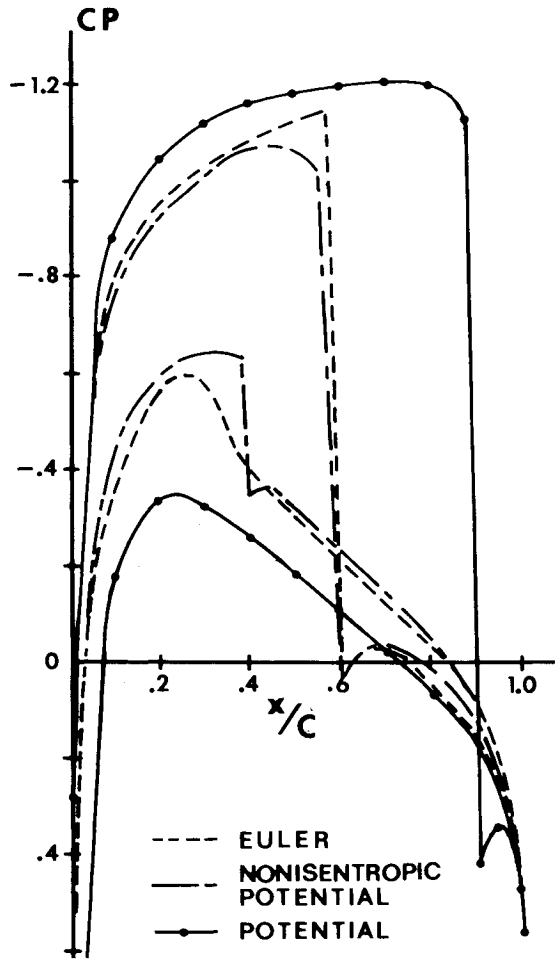


**Fig. 6 Comparison of pressure coefficients for isentropic potential, nonisentropic potential, and Euler approximations ($M_\infty = 0.80$, $\beta_\infty = 1.25$ deg).**

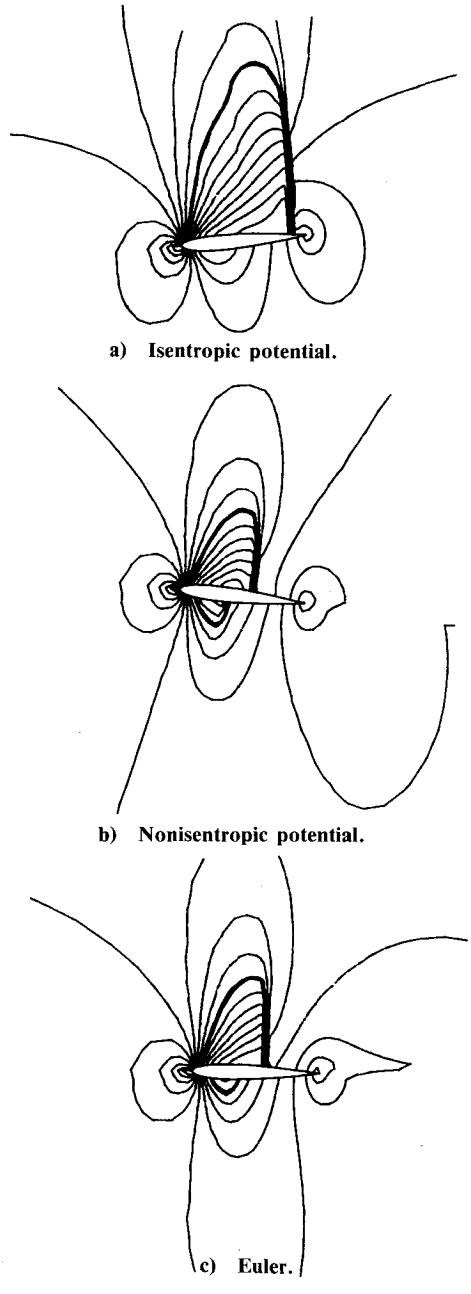


**Fig. 7 Mach contours for isentropic potential, nonisentropic potential, and Euler approximations ($M_\infty = 0.80$, $\beta_\infty = 1.25$ deg, $\Delta M = 0.050$).**

sonic flows.[9] The computational grid employed for both cases and for all three types of solutions is shown in Fig. 2.

This C-type grid was chosen instead of an O-type grid since the distribution of grid points near the narrow nonisentropic region past the shocks was found to be better suited for Euler calculations. For the same flow domain, more grid points are required with C-grids; thus, the convection of entropies can be calculated more accurately due to a better resolution around the dividing streamline. This grid was generated by using a block-based finite element mesh generation scheme specifically developed for complex geometries.[10] It consists of a total of 3050 four-noded elements with 74 grid points placed on the surface of the airfoil. The far-field boundaries extend radially to 10 chord lengths in the upstream and transverse directions and 5 chord lengths longitudinally in the downstream direction.

For both test cases, a potential solution was obtained first. As discussed previously, in this approximation the velocity field is expressed by the velocity potential function only. The mass density is calculated by assuming the entropy to be constant in Eq. (8) across the shock as well as in the entire flowfield. As a second step, an irrotational but nonisentropic solution is obtained. This still corresponds to the use of Clebsch representation in Eq. (12). However, the density is determined from Eq. (8) including the entropy variations for the fluid particles in the nonisentropic flow region (Fig. 3). The entropy distribution is calculated across the shock from the Rankine-Hugoniot relationship. After the shock, with known $\alpha$ values from Eq. (4), the relationship $S = S(\alpha)$ is used for the fluid particles emanating from the shock. Finally, a full Euler solution was obtained by solving Eqs. (2-4) together with the Rankine-Hugoniot relationship and Eqs. (1), (6), (8), and (9). In the supersonic pockets, where the density is upwinded, all three approximations require the solution of the potential equation only.

The numerical results for the first test case ($M_\infty = 0.8$, $\beta_\infty = 1.25$ deg) are shown in Figs. 4-6. Figure 4 illustrates the pressure distribution over the airfoil as obtained by the present analysis and as compared with other representative results in the literature. Figure 5 shows the same comparison for the Euler solutions. Finally, the obtained numerical results for the potential, nonisentropic potential, and Euler solutions are compared in Fig. 6. Also, a similar comparison is made in terms of the Mach contours in Fig. 7. One can observe a major change in the solution when density is computed by including the entropy changes across the shock. Once the full Euler equations are solved, there is yet a further but smaller change in the solution.

Similar results are obtained for the second test case with $M_\infty = 0.85$ and $\beta_\infty = 1.0$ deg. Figures 8 and 9 illustrate the

comparisons of potential and Euler solutions, respectively, with those in Ref. 9. The comparison of the three different types of solutions are again illustrated in Figs. 10 and 11 in terms of the surface pressure distributions and Mach contours, respectively. The upwinding of the density in the supersonic pocket was introduced using the same formulation in all three cases and only the conservation of mass equation is needed in this region. The effective upwinding was different in all cases, however, since the calculated Mach numbers are lower in the Euler solution then in the potential solution.

Another important observation made during the computation of the above two test cases is the importance of the artificial viscosity in the conservation of mass equation at all three steps. The accuracy of the solutions in terms of locating the shock and the supersonic pocket strongly depends on the accurate solution of the isentropic potential equations inside the pocket. No entropy was generated in this region. However, the solution inside the supersonic pocket determines the strength and location of the shock which is the sole source of entropy generation. Figure 12 illustrates the material lines and contours of nondimensionalized vorticity/pressure values,

$$\bar{\zeta} = (\zeta C/a_0)/(p/p_0) \tag{38}$$

where $C$ is the chord length of the airfoil and $a_0$ and $p_0$ the stagnation values of the speed of sound and the pressure, respectively.

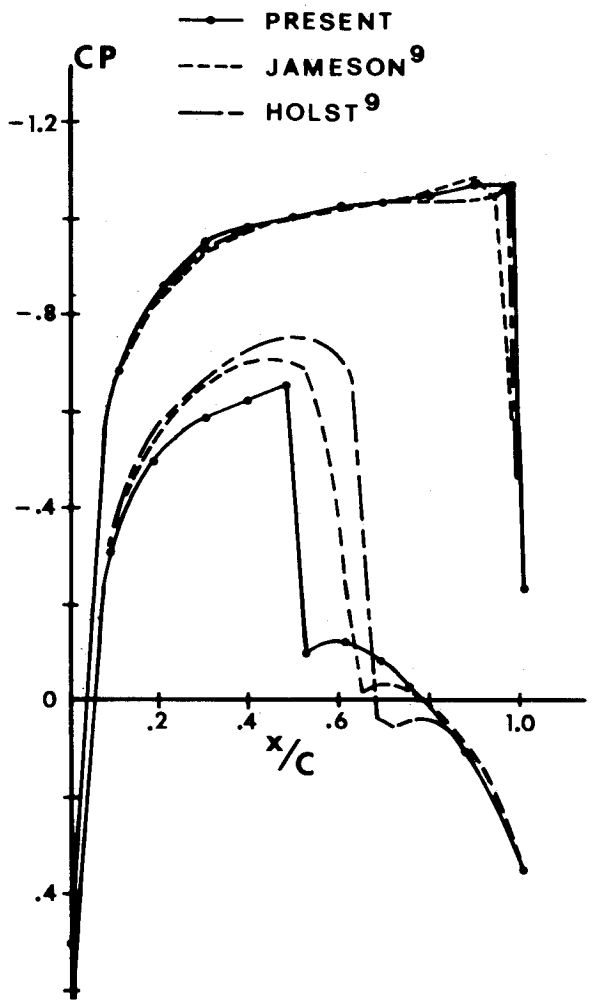


Fig. 8 Comparison of pressure coefficients for isentropic potential solutions ($M_\infty = 0.85$, $\beta_\infty = 1.0$ deg).

As can be seen from these results, any vorticity generated at the shock is convected with no diffusion. The scheme is second-order accurate in the subsonic nonisentropic region behind the shock with no artificial diffusion effects. The same behavior can be observed by comparing the profiles of $\bar{\zeta}$ at the shock, at the trailing edge, and at the downstream boundary of the grid, as shown in Fig. 13. Both the vorticity and pressure are computed here from the calculated velocity field and the entropy distribution. Finally, in Fig. 14, a com-

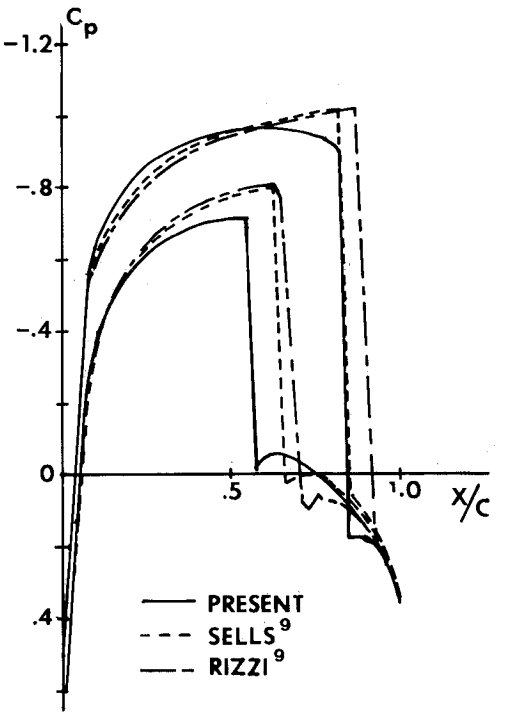


Fig. 9 Comparison of pressure coefficients for Euler solutions ($M_\infty = 0.85$, $\beta_\infty = 1.0$ deg).

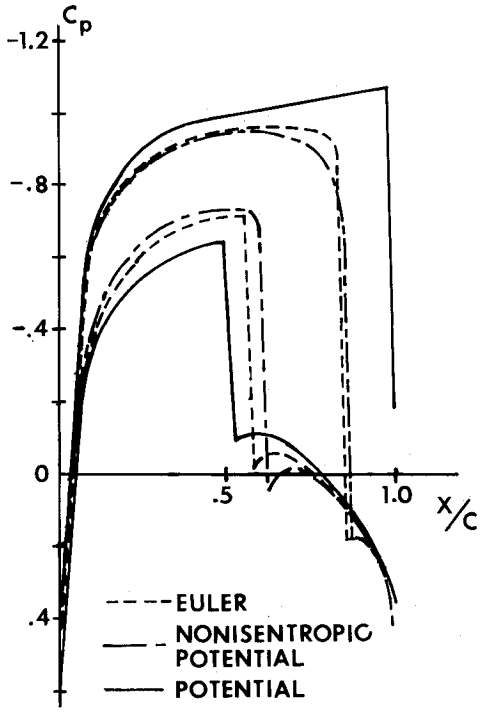


Fig. 10 Comparison of pressure coefficients for isentropic potential, nonisentropic potential, and Euler approximations ($M_\infty = 0.85$, $\beta_\infty = 1.0$ deg).

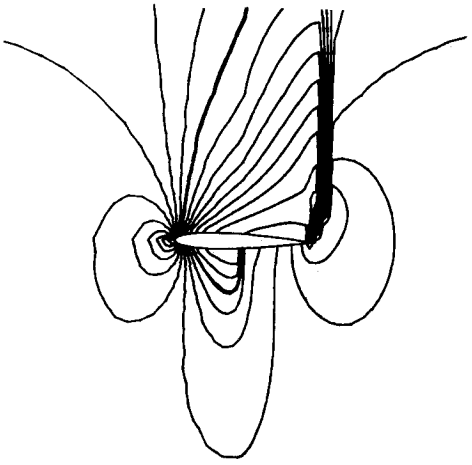

a) Isentropic potential.

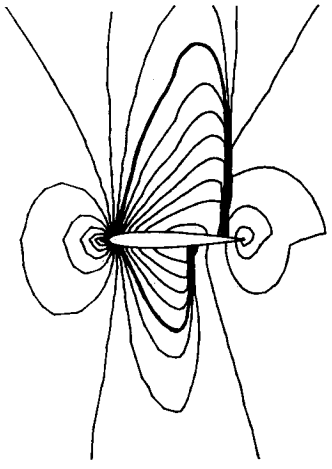

b) Nonisentropic potential.

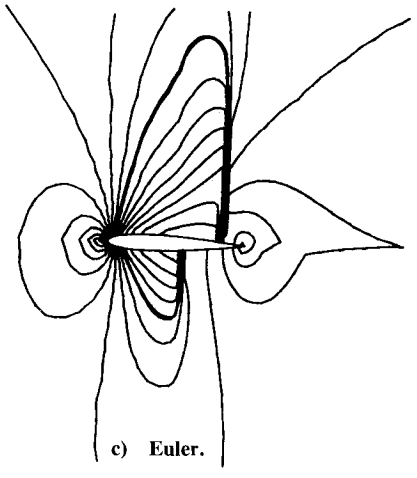

c) Euler.

**Fig. 11 Mach contours for isentropic potential, nonisentropic potential, and Euler approximations ($M_\infty = 0.85$, $\beta_\infty = 1.0$ deg, $\Delta M = 0.050$).**

parison of velocity profiles for all three approximations is made at the downstream. As can be seen from the velocity distributions near the dividing streamline, there are significant differences among the results of three cases.

For the results presented, the isentropic potential solutions were obtained using the uniform flow conditions as initial guesses, which subsequently were used as initial conditions to the nonisentropic potential solutions. The nonisentropic potential solutions were then used as initial guesses to the

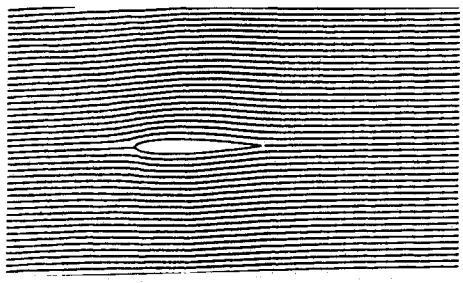

a) Material lines ($\Delta\alpha = 0.050$).

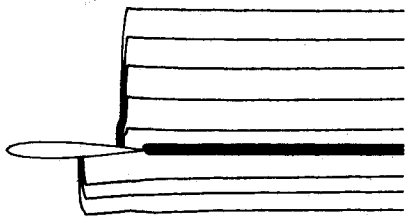

b) Nondimensionalized vorticity/pressure contours ($\Delta\tilde{\zeta} = 0.015$).

**Fig. 12 Material lines and the nondimensionalized vorticity/pressure contours around the airfoil ($M_\infty = 0.85$, $\beta_\infty = 1.0$ deg).**

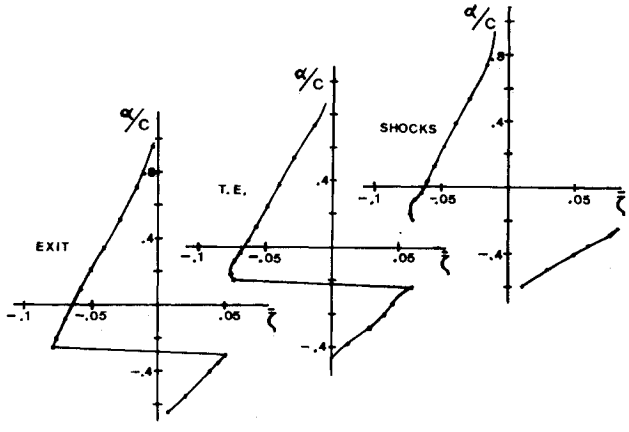


**Fig. 13 Comparison of nondimensionalized vorticity/pressure distribution at the shock, at the trailing edge, and at the downstream boundary ($M_\infty = 0.85$, $\beta_\infty = 1.0$ deg).**

full Euler solutions. It is also possible to directly obtain the nonisentropic potential and full Euler solutions starting from the uniform initial conditions. In fact, it has been observed that the number of iterations required for convergence to the steady state is rather insensitive to the choice of initial solutions. Hence, for cases where only an Euler solution is required, it is more efficient to start from uniform flow conditions directly and to omit the calculation of intermediate approximations.

The computational effort needed for a nonisentropic potential solution is in the same order as an isentropic potential solution. It is only 4-6% higher than an isentropic potential solution. Since all three equations have to be solved successively for a full Euler approximation and a greater number of iterations are required for convergence, an Euler solution generally requires an order of magnitude more computational effort. On the other hand, the comparison of the size of nonisentropic and isentropic regions in Fig. 3 suggest that by selectively solving only the conservation of mass equation in the isentropic regions and the full Euler equations in only the nonisentropic regions, one can achieve considerable savings in the computations.

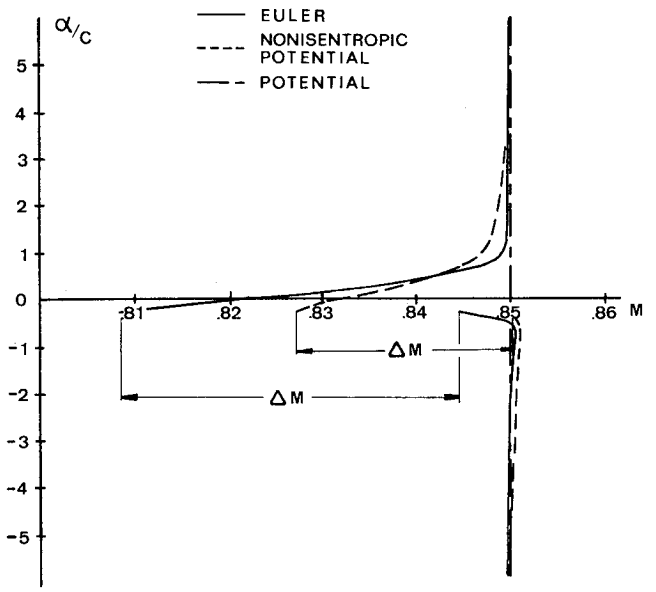


**Fig. 14 Comparison of velocity profiles at the downstream boundary of the grid as obtained from isentropic potential, nonisentropic potential, and Euler approximations ($M_\infty = 0.85$, $\beta_\infty = 1.0$ deg).**

## Conclusions

A previously developed finite element computational scheme is extended to treat lifting airfoils in transonic regimes. The method which uses a Clebsch-variable form of Euler equations is found particularly advantageous in evaluating the effects of different approximations used in transonic flows. Using the same computational procedure and the same computational grid, the solutions obtained from potential, nonisentropic potential, and Euler equations were compared. The separate effects of including entropy variations and rotationalities can be determined systematically using a unified approach. For all approximations, the same density upwinding technique is employed in supersonic regions. Since no artificial viscosity is used in subsonic regions, the convection of entropies and vorticities can be calculated accurately.

A cut in the grid that extends from the airfoil trailing edge to the downstream boundary is used to model the Kutta condition and the dividing streamline in the nonisentropic region. Assuming small angles of attack, this cut was extended horizontally. A modification in the grid may be needed for the alignment of the grid points on cut with the actual dividing streamline when higher angles of attack are involved.

For the test cases considered, it has been observed that the shock strengths and positions change considerably once the entropy changes are included. Rotationalities alter the solutions only slightly. Although the capability of solving the full Euler equations across the shocks and around the trailing edge may still be desirable for some transonic flow problems, the nonisentropic potential approximation offers an efficient alternative to the problem with a slight compromise in accuracy.

The jump in the magnitude of velocity at the exit is significant even for small angles of attack. The developed scheme is also well suited to predicting this jump.

## Acknowledgments

This research was sponsored by the U.S. Air Force Office of Scientific Research under Contract F49620-83-K-0034. Support provided by the IUPUI and Indiana University Computer Centers is gratefully acknowledged.

## References

[1]Rizzi, A., "Spurious Entropy Productions and Very Accurate Solutions to the Euler Equations," AAIA Paper 84-1644, June 1984.

[2]Hafez, M. M. and Lovell, D., "Numerical Solution of Transonic Stream Function Equation," AIAA Paper 81-1017, June 1981.

[3]Klopfer, G. H. and Nixon, D., "Nonisentropic Potential Formulation for Transonic Flows," *AIAA Journal*, Vol. 22, June 1984, pp. 770-776.

[4]Hafez, M. M. and Habashi, W. G., "Conservative Calculations of Nonisentropic Transonic Flows," AIAA Paper 84-1182, June 1984.

[5]Ecer, A. and Akay, H. U., "A Finite Element Formulation of Euler Equations for the Solution of Steady Transonic Flows," *AIAA Journal*, Vol. 21, March 1983, pp. 343-350.

[6]Akay, H. U. and Ecer, A., "Application of a Finite Element Algorithm for the Solution of Steady Transonic Euler Equations," *AIAA Journal*, Vol. 21, Nov. 1983, pp. 1518-1524.

[7]Akay, H. U. and Ecer, A., "Finite Element Formulation of Rotational Transonic Flow Problems," *Finite Elements in Fluids*, edited by R. H. Gallagher et al., John Wiley & Sons, New York, 1984, pp. 173-195.

[8]Ecer, A. and Akay, H. U., "Investigation of Transonic Flow in a Cascade Using the Finite Element Method," *AIAA Journal*, Vol. 19, Sept. 1981, pp. 1175-1182.

[9]Rizzi, A. and Viviand, H. (eds.), *Numerical Methods for the Computation of Inviscid Transonic Flows with Shock Waves*, Friedr. Vieweg & Sohn, Braunschwerg/Wiesbaden, FRG, 1981.

[10]Ecer, A., Spyropoulos, J., and Tuncer, I. H., "A Block-Structured Finite Element Grid Generation Scheme for the Analysis of Three-Dimensional Transonic Flows," AIAA Paper 84-0004, Jan. 1984.